

Vortex-Stretching based Large Eddy Simulation Framework for Wind Farms

Jagdeep Singh^{1,*}, Jahrul Alam¹

*Department of Mathematics and statistics
Memorial University of Newfoundland, St. John's, Canada- A1C 5S7*

Abstract

In large wind farms, wake distribution behind a wind turbine causes a considerable reduction of wind velocity for downstream wind turbines, resulting in a significant amount of power loss. Therefore, it is very crucial to predict wind turbine wakes efficiently. Thus, we propose a large-eddy simulation (LES) methodology, which takes the vorticity stretching to model transients in wind turbine wakes. In addition, we present an improved actuator disk model, which accounts for two-way feedback between the atmosphere and the wakes. First, we show that the vertical profile of the mean wind predicted with the new model has an excellent agreement with experimental measurements. Next, we validate the predicted Reynolds stresses against wind tunnel data and show that the dispersive stresses account for about 40% of Reynolds stresses. Finally, we show that the proposed LES method accurately predicts the characteristics of wind turbine wakes. Comparing the LES results with previously reported data, we have found that the new LES framework accurately predicts the flow statistics in both the near-wake and the far-wake regions.

Keywords: Actuator disk model, Large eddy simulation, Vortex-Stretching, Wind farm, Wind turbine wakes

1. INTRODUCTION

Large wind farms are increasing worldwide to mitigate climate change and accomplish sustainable developments [1]. However, the movement of air currents through wind farms is not well understood [2, 3]. Large-eddy simulations (LES) of wind farms provide critical data that could help wind energy developers increase energy production [4, 5, 6]. The development of technologies for reducing the power losses caused by wind turbine wake is one of the most challenging topics [7]. LES techniques can simulate details of the tip vortices and wind turbine blades. However, computational resources are insufficient for such a highly resolved LES of wind farms [8]. Predictions of near turbine regions with state-of-the-art LES methods differ significantly [9]. Flattened near wake profiles and sharp deviation from the ground surface are typically seen in the classical actuator disk model (ADM), where the local variation of the thrust across the rotor is neglected. Such errors are adequately controlled with an actuator line model if the nacelle, rotational effects

*Corresponding Author.

Email addresses: jagdeeps@mun.ca (Jagdeep Singh), alamj@mun.ca (Jahrul Alam)

of turbines, tip vortices, and the atmospheric boundary layer (ABL) region below the rotor bottom are sufficiently resolved [10]. However, neither of such methods is appropriate for LES of utility-scale large wind farms in which two-way feedback of atmospheric boundary layer becomes essential [5, 6, 11]. Therefore, a scale-adaptive LES using an improved actuator disk model can be a promising solution to balance the efficiency and accuracy. In this work, we evaluate and demonstrate the predictive capabilities of a scale-adaptive LES model for simulating wind farms using wind tunnel measurements.

Wind farms extract energy from the lower part of the ABL, where turbulence is highly anisotropic due to different dynamical processes occurring in that region [12, 13]. One such process is vorticity production due to the stretching of fluid elements [14, 15]. Thus, this article aims to present a scale-adaptive turbulence model for the LES of wind farms. In LES, one seeks to model the residual stress (τ) and, consequently, the energy flux (Π). These two quantities (τ and Π) account for the errors associated with the missing flow physics (due to limitations in measurements or LES) in the resolved (or measured) quantities. Vortex stretching and strain self-amplification are the two most critical dynamical mechanisms in wakes behind wind turbines [16]. Therefore, we propose considering a scale-adaptive turbulence model for the residual stress using the concept that vortex-stretching is a primary mechanism for the downscale cascade of energy. Another goal is to improve the wake model of turbines by considering that the actuation of a turbine can form a spherical canopy of stresses around the rotor.

1.1. Related work

LES is currently one of the most efficient turbulence modelling approaches, which has substantially impacted the remarkable growth of wind energy worldwide [5, 3]. LES is of great significance in wind energy and the atmospheric science sector in studying the complex interaction of atmospheric turbulence and large wind farms [17, 10, 4, 5, 6].

In LES, a closure model for the residual stress τ_{ij} enables the accurate prediction of turbulence statistics and local energy cascade rate $\Pi(\mathbf{x}, t)$. The most common parameterization for residual stresses in LES is the Smagorinsky model [18]. The Smagorinsky length scale is $l_s = C_s \Delta$, where C_s is the model coefficient and Δ is the grid spacing. Existing methods for *a priori* determination of C_s and its dependency on local conditions such as atmospheric stability, surface-normal distance, and mean shear are complex tasks and dependent on advanced knowledge of turbulence theory. The model coefficient need adjustments in the region of large turbulence anisotropy [19, 20, 21, 22, 23]. The dynamic Smagorinsky model is a procedure [24] to estimate variations of the model coefficient C_s . This procedure is based on the scale-invariance assumption and requires test-filter operations and an average over the homogeneous flow direction. Averaging over a homogeneous flow direction is not reasonable in the case of complex geometries. Ref [25] adapted the averaging along flow path lines known as Lagrangian averaging to alleviate this problem. A scale-dependent dynamic model was formulated by [26] to overcome the scale-invariance assumption. In the scale-dependent Lagrangian model, the predicted logarithmic wind profiles were better than both the dynamic Smagorinsky and classical Smagorinsky models in the case of neutrally stratified atmospheric boundary layer flow over a homogeneous flat surface.

Furthermore, Refs [27, 28] evaluated the Lagrangian scale-dependent model for heterogeneous flat surfaces and, consequently, [29] performed the Lagrangian scale-dependent model on a two-dimensional sinusoidal hill. Predicting momentum and turbulence kinetic energy (TKE) becomes highly accurate if LES adequately resolves the vortical and straining motion in wind turbine wakes

[16]. As a result, choosing a subgrid-scale model may not be a determining factor in the LES of wind farms. However, in the LES of a wind farm, resolving the large eddies in the surface layer (10% of ABL) and the near-wake region of a wind turbine, *e.g.*, helical tip vortices, is not possible with computational resources in hand.

The actuator disk model (ADM) and actuator line model (ALM) are the most popular methodology to parameterize turbine-induced forces. They are extensively used in large-eddy simulations of wind farms by many researchers [see 17, 10, 30, 5, 31, 9]. The actuator disk model (ADM) does not require resolving the boundary layer, and thus it significantly reduces the computational cost. In contrast, the actuator line model (ALM) requires almost 40 grid points along each line of ALM to capture the tip vortices [16]. The actuator disk model only requires 5 – 10 grid points across the rotor diameter. However, ADM could not produce the tip vortices at this resolution and could not fully capture the vortex shedding behind the disk, and consequently, power is over-predicted by more than 10% [32]. In addition, the wind turbine structures such as blades, hub, and nacelle [33], strongly influence the flow fields in *near-wake*, which leads to a significantly complex, three-dimensional turbulent flow in this region.

On the other hand, the flow field in the *far-wake* is less likely to have a significant influence from wind turbine structures. Thus, the actuator disk theory predicts the *far-wake* mean flow field with the global parameters such as momentum, power coefficient, and inflow condition. Researchers proposed several modifications to improve the actuator disk model; for example, [30] used a modified ADM, which applies thrust and torque to the incoming flow. The results of this modified ADM were in good agreement with the experimental observations. However, this approach requires *a priori* knowledge of lift and drag coefficients. For ADM and ALM, Ref [9] also investigated the influences of the wind turbine structures, *e.g.*, nacelle and tower. Numerical tests of ADM and ALM incorporating structural effects in the LES indicate an excellent correlation with the experimental data. Nevertheless, it increases the complexity of the numerical simulation.

1.2. Outline

The organization of this article is as follows. First, Sec 2 provides a brief outline of the fundamentals of the parameterization of turbulence and turbines and lays a general-purpose formulation of the algorithms, making them applicable to any existing research LES code. Next, in Sec 3, we summarize the findings of our numerical simulations: an isolated wind turbine and an array of 30 wind turbines. In particular, we employ wind tunnel measurements to understand how to extend the actuator disk theory for accurate modeling of wind turbine wakes. Finally, Sec 4 summarizes and discusses key findings and highlights potential future extensions, some of which are currently underway.

2. Gaussian actuator disk model for LES of wind farms

2.1. Large eddy simulation framework

The filtered version of continuity and momentum equations are:

$$\frac{\partial \bar{u}_i}{\partial x_i} = 0, \quad (1)$$

$$\frac{\partial \bar{u}_i}{\partial t} + \bar{u}_j \frac{\partial u_i}{\partial x_j} = -\frac{\partial \bar{p}}{\partial x_i} - \frac{\partial \tau_{ij}}{\partial x_j} + f_i \chi(\mathbf{x}, t), \quad (2)$$

where \bar{u}_i ($i = 1, 2, 3$) is the filtered velocity component in the streamwise (x_1), spanwise (x_2) and surface-normal direction (x_3), respectively. The function $\chi(\mathbf{x}, t)$ is either 0 or 1 depending on where the body force is applied. The residual (sub-filter) stress tensor $\bar{\tau}_{ij} = \overline{u_i u_j} - \bar{u}_i \bar{u}_j$, accounts for the effects of small-scale motions smaller than the filter width Δ_{les} . The following section discusses parameterization techniques for the subgrid-scale turbulence and wind turbine.

2.2. Turbulence modelling

2.2.1. Smagorinsky model

Among various models for subgrid-scale turbulence, the Smagorinsky model is used widely [18], where the stress tensor τ_{ij} appeared in Eq (2) is represented as

$$\tau_{ij} - \frac{1}{3}\tau_{kk}\delta_{ij} = -2\nu_\tau \mathcal{S}_{ij}. \quad (3)$$

Here, $\nu_\tau(\mathbf{x}, t) = C_s \Delta_{les}^2 (2\mathcal{S}_{ij}\mathcal{S}_{ij})^{1/2}$ is the eddy viscosity, δ_{ij} represents kronecker delta and $\mathcal{S}_{ij} = 1/2(\mathcal{G}_{ij} + \mathcal{G}_{ji})$ is the symmetric part of the velocity gradient tensor $\mathcal{G}_{ij} = \partial u_i / \partial x_j$ and the model coefficient $C_s = (1/\pi)(3K_c/2)^{-3/4}$ is known as the Smagorinsky constant. For a Kolmogorov constant of $K_c \approx 1.4$, one gets $C_s \approx 0.18$. At high Reynolds number, the production of vortices becomes highly intermittent in space and time [24]. It is thus necessary to consider the Leonard (or resolved stress) $\tau_{ij}^L = \widetilde{\bar{u}_i \bar{u}_j} - \widetilde{\bar{u}_i} \widetilde{\bar{u}_j}$ to introduce spatio-temporal variability of the Smagorinsky coefficient $C_s(\mathbf{x}, t)$. This approach is known as the dynamic Smagorinsky model, in which $C_s(\mathbf{x}, t)$ becomes negative, thereby leading to numerical instability. However, several sophisticated models exist as a workaround, making the dynamic Smagorinsky model a reliable scheme. Note that the energy flux of the dynamic Smagorinsky model takes the following form:

$$\Pi = C_s^2(\mathbf{x}, t) \Delta_{les}^2 2^{3/2} (\mathcal{S}_{ij}\mathcal{S}_{ij})^{3/2}, \quad (4)$$

Clearly, the dynamic Smagorinsky model does not directly account for the production of vorticity in wind turbine wakes and the associated intermittency of turbulence. It is important to note that the tip-speed ratio, $\lambda = |\boldsymbol{\omega}|D/(4u_d)$, of a turbine of rotor diameter (D), relates the vorticity ($\boldsymbol{\omega}$) with the local fluid velocity u_d . Thus, the rotation of turbines influences the momentum conservation law *via* the vortex stretching term $\mathcal{S}_{ij}\omega_j$ that appears in the vorticity form of the Navier-Stokes equation. Consequently, wind turbines contribute to the dynamical evolution of the enstrophy ($0.5|\boldsymbol{\omega}|^2$) *via* vorticity stretching $\omega_i \mathcal{S}_{ij} \omega_j$. Readers may find a technical details of vortex stretching theory in Chapter 5 of Ref [14]. Below, we present our development of a subgrid model that accounts for the effects of vortex stretching.

2.2.2. Vortex-stretching based scale-adaptive subgrid model

Consider the truncated Taylor-series expansion

$$\bar{u}_i(\mathbf{x}, t) = \widetilde{\bar{u}_i}(\mathbf{r}, t) + (\mathbf{x} - \mathbf{r})\mathcal{G}_{ij}, \quad (5)$$

where $\mathbf{x} = \mathbf{r} + \alpha\Delta_{les}$. Assuming the solution of Navier-Stokes equations remains smooth and continuous at high Reynolds number, one can express the Leonard stress approximately as

$$\tau_{ij}^L = c_k \Delta_{les}^2 \mathcal{G}_{ik} \mathcal{G}_{jk}. \quad (6)$$

In the literature, Eq (6) is known as the gradient model, a complete discussion of which is outside the scope of the current research. Using Eq (6), we get the following form of the energy flux,

$$\Pi = C_k \Delta^2 \left[-\mathcal{S}_{ik} \mathcal{S}_{kj} \mathcal{S}_{ji} + \frac{1}{4} \omega_i \omega_j \mathcal{S}_{ij} \right], \quad (7)$$

where $\omega_i = \epsilon_{ijk} \mathcal{G}_{kj}$ is the vorticity vector and $\mathcal{S}_{ik} \mathcal{S}_{kj} \mathcal{S}_{ji}$ is the skewness of the filtered strain tensor. Comparing Eq (4) and Eq (7), one finds that the use of Eq (6) as a subgrid model would make the energy flux depend directly on strain skewness and vorticity stretching.

After some algebraic manipulation, we can write

$$-\frac{1}{2} \tau_{ij}^{Ldev} \tau_{ji}^{Ldev} = -\frac{1}{4} \left[\mathcal{S}_{ij} \omega_j \mathcal{S}_{ik} \omega_k + \frac{1}{3} (\mathcal{G}_{ij} \mathcal{G}_{ji})^2 \right]. \quad (8)$$

Following Deardorff's modification of Smagorinsky model, the subgrid scale stress in Eq (3) can be given by

$$\tau_{ij} - \frac{1}{3} \tau_{kk} \delta_{ij} = c_k \Delta_{les} \sqrt{k_{sgs}} \mathcal{S}_{ij}. \quad (9)$$

Based on dimensional consideration, an algebraic model for the subgrid-scale turbulence kinetic energy may take the following form:

$$k_{sgs} = \frac{\Delta_{les}^2 \left(\frac{1}{2} \mathcal{S}_{ij} \omega_j \mathcal{S}_{ik} \omega_k + \frac{1}{6} (\mathcal{G}_{ij} \mathcal{G}_{ji})^2 \right)^3}{\left[(\mathcal{S}_{ij} \mathcal{S}_{ij})^{5/2} + \left(\frac{1}{2} \mathcal{S}_{ij} \omega_j \mathcal{S}_{ik} \omega_k + \frac{1}{6} (\mathcal{G}_{ij} \mathcal{G}_{ji})^2 \right)^{5/4} \right]^2}. \quad (10)$$

Note that the subgrid model Eq (9) implicitly adapts the energy flux as the characteristic length scale of turbulence dissipation varies locally. Recent work of [34, 15, 35] evaluated the scale-adaptive LES model, Eq (9), in the case of isotropic turbulence, and atmospheric boundary layer flow over urban and hilly terrain. In this research, we consider an improved actuator disk model and show that our scale-adaptive LES method adequately captures the near turbine dynamics.

To approximate the parameter c_k , we consider fixed values of the Smagorinsky constant

$$C_s(\mathbf{x}, t) = \frac{1}{\pi} \left(\frac{3K_c}{2} \right)^{-3/4}$$

and the Kolmogorov constant $K_c = 1.4$ in Eq (4). Then, we obtain c_k by equating the energy flux given by Eq (4) to the energy flux obtained by employing Eq (9). This is equivalent to mimicking the effects of dynamical variations of $C_s(\mathbf{x}, t)$ via the stretching of vortices. Based on LES of decaying homogeneous isotropic turbulence for Reynolds numbers up to 10^8 (using the localized dynamic Smagorinsky model [34]), we found that $c_k = 0.325 \pm 0.035$. Thus, a fixed value of $c_k = 0.325$ is considered in this article.

2.3. Wind turbine parameterization

In this section, we extend classical ADM by considering that the actuation of a turbine forms a spherical canopy of stresses around the rotor. The actuator disk theory considers the momentum

principle in a stream tube around a turbine, in which the thrust force is

$$f = -\frac{1}{2}\rho C'_t u_d^2 A_c. \quad (11)$$

This thrust is applied as a momentum sink due to fluid elements passing over the rotor disk. The streamwise velocity u_d is averaged over the actuator disk and related to the upstream undisturbed velocity (U_∞) such that $u_d = (1 - a)U_\infty$, where a is the axial induction factor, A_c is the frontal area, and $C'_t = C_t/(1 - a)^2$ is a modified form of the thrust coefficient C_t . This model leads to a flattened near-wake profile because it does not account for the wind speed variation across the rotor. We have considered the following two developments. For a pedagogical reason, these two formulations will be referred to as ‘model A’ and ‘model B’, respectively.

According to the blade element momentum theory, the power coefficient $C_p = 4a(1 - a)^2$ accounts for the wind power efficiency. However, the dynamic load is related to the turbulent intensity in wakes [36]. Thus, in model A, we consider the following form of the thrust force

$$f_i(\mathbf{x}, t) = -\frac{1}{2}\rho C'_t A_c u_d \bar{u}_i(\mathbf{x}, t), \quad (12)$$

in which the instantaneously resolved velocities $\bar{u}_i(\mathbf{x}, t)$ in all three directions are considered in Eq (12). This force is projected onto the numerical domain using a three-dimensional Gaussian kernel

$$G(r) = \frac{1}{\sqrt{2\pi}\Delta_G} \exp\left(-\frac{1}{2} \frac{r^2}{\Delta_G^2}\right),$$

where r represents distance from the centre of the actuator disk to the point where the influence of turbine is assumed, Δ_G is the width of Gaussian kernel. Then the total thrust force (F_T) takes the following form

$$F_T = \frac{1}{\Delta v} [f_i(\mathbf{x}, t) \otimes G(r)], \quad (13)$$

where the symbol ‘ \otimes ’ is the convolution between the two functions, and Δv is the volume of a grid cell.

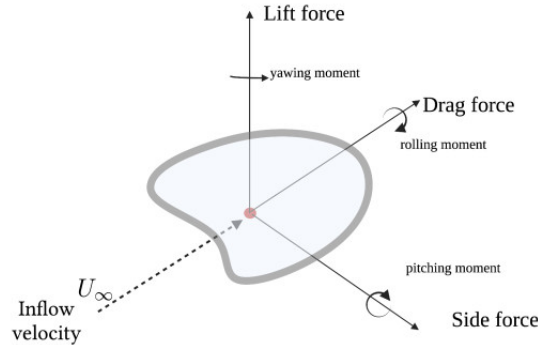


Figure 1: Schematic diagram illustrates the forces and moments acting on an arbitrary object when immersed in a fluid flow.

In model B, we consider the fluid dynamics point of view in which a solid body of an arbitrary

shape is immersed in a fluid, as shown in Fig 1. An immersed body will experience forces and moments from all three principal axes. Let us assume that the body is immersed in a fluid flow, and the incoming flow stream is parallel to the main chord line of the body and has symmetry about the lift-drag axis such as cylinder, sphere, wings, etc. The body will then only experience a drag force. This approach considers the momentum principle in a control volume around a wind turbine. Considering the loss of momentum and pressure due to frictional effects, we arrive at the following form of total drag experienced by the turbine:

$$f_i(\mathbf{x}, t) = -C_\nu \bar{u}_i(\mathbf{x}, t) - C'_t |\bar{\mathbf{u}}| \bar{u}_i(\mathbf{x}, t), \quad (14)$$

where $|\bar{\mathbf{u}}| = \bar{u}_i \bar{u}_i$ is a function of (\mathbf{x}, t) . Here, C_ν is the viscous drag coefficient, and C'_t is the coefficient of pressure drag. We have applied the thrust force (given by Eq 14) over a spherical canopy with a center that coincides with the center of a rotor similarly as in model-A but without using a Gaussian kernel.

3. RESULT ANALYSIS

The scale-adaptive LES framework discussed in this article has been implemented in an updated version of the (collocated grid) Navier-Stokes solver that was detailed previously by [35]. Previous utilization of the code investigated the interaction of geophysical turbulent flow over an array of wind turbines using classical ADM [11], as well as turbulent flow over the Askervein hill, UK [15]. Here, we investigate the new development of the Gaussian actuator disk model of the wind turbine and compare the numerical results against the experimental data.

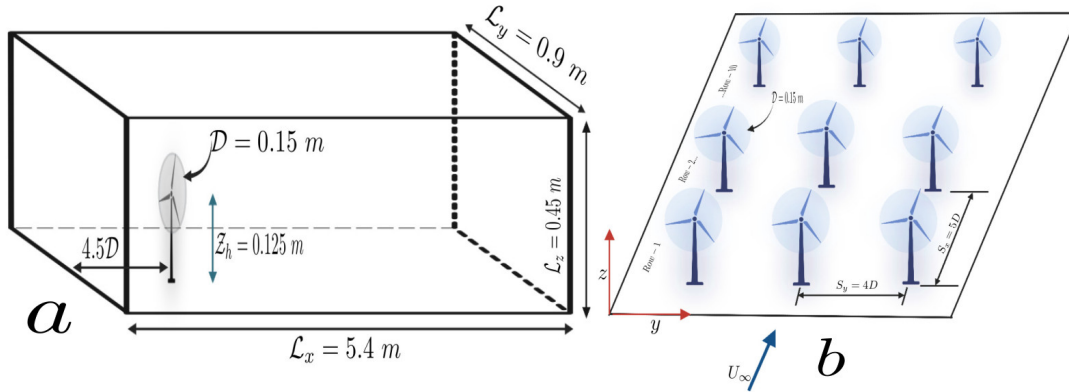


Figure 2: **a)** The computational domain $\mathcal{L}_x \times \mathcal{L}_y \times \mathcal{L}_z = [5.4 \times 0.9 \times 0.45] \text{ m}^3$, which represents the simulated part of the wind tunnel test section. **b)** The layout of an array of 10×3 wind turbines in the computational domain $\mathcal{L}_x \times \mathcal{L}_y \times \mathcal{L}_z = [14.4 \times 1.8 \times 0.675] \text{ m}^3$. Only first two and the last row of the array 10×3 are shown for clarity. The streamwise and spanwise spacing between wind turbines are $\mathcal{S}_x = 5D$ and $\mathcal{S}_y = 4D$, respectively.

Fig 2a-b represents the test sections of the wind-tunnel experiment [37, 38], which have been simulated in the present work. The rotor diameter and the hub height of the turbine are 0.15 m and 0.125 m, respectively. The data of the first experiment consists of the velocity profiles (and Reynolds stresses) on the vertical mid-plane at 8 locations: $x/D = -1$, $x/D = 2$, $x/D = 3$,

$x/D = 5, x/D = 7, x/D = 10, x/D = 14, x/D = 20$, where $x/D = 0$ is the center of the turbine which is located at $4.5D$ from the inlet plane. Fig 3a compares the vertical profile of the streamwise velocity between the experimental data at $x/D = 2$ and the corresponding LES result using classical ADM [8]. As discussed in the introduction, the wind profile from the classical ADM has been flattened. More specifically, sharp deviation is seen in the boundary layer below the rotor bottom. Fig 3b shows the velocity deficit ($\Delta U = |u_{ref} - u_{exp}|$) of the experimental data at $x/D = 2$, where u_{ref} is the streamwise velocity at the inlet of the wind-tunnel test section. Using the curve-fitting tool of MATLAB, we observe that the experimental velocity deficit shows a perfect agreement with a Gaussian profile (Fig 3b). The experimental data suggest the validity of the assumptions of the Gaussian profile of the thrust across the actuator disk in model A. This observation is particularly relevant to generalizing the velocity deficit in classical non-rotating ADM and developing a model that accounts for the rotational effects of the disk [36].

The second set of experimental data is velocity profiles (and Reynolds stresses) on the vertical mid-plane of the wind tunnel test section for a 10×3 array of wind turbines at 4 locations: $x/D = 1, x/D = 2, x/D = 3, x/D = 4$ behind each row of wind turbines. A Gaussian pattern of the near turbine wake was also observed for this set of experimental data.

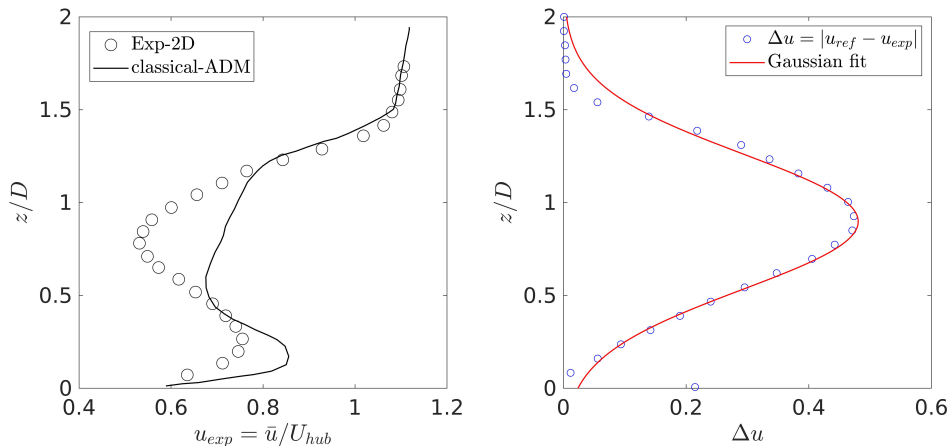


Figure 3: **a)** A comparison of the wind tunnel measurement at $x/D = 2$ with the corresponding LES result of [8] using classical-ADM. **b)** A comparison of velocity deficit in the experimental data [37] with a Gaussian curve.

3.1. Gaussian actuator disk model

A parametric study of the Gaussian actuator disk model was considered for 11 test cases (see Table 1). In these tests, the aspect ratio of the horizontal grid spacing to the vertical grid spacing was varied.

3.1.1. Mesh sensitivity analysis with an isolated turbine

Table 1 reports the number of grid points N_{x_2} and N_{x_3} across the actuator disk in spanwise and vertical directions, respectively. This study considers a decreasing sequence of average grid spacing Δ/D in the range $[0.45, 0.079]$ for both model A and model B (see, Table 1). Numerical data were sampled at eight streamwise locations following the aforementioned wind-tunnel experiment. Vertical profiles of the mean streamwise velocity are shown in Fig 4 and Fig 5 for model A and model B, respectively. Flattened profiles are seen only for the two coarsest resolution cases: (M1,

M2) for model A and (M6, M7) for model B. This behaviour is quite similar to the predictions made with the classical ADM (*e.g.*, see Refs [8] and [9]). The velocity profiles for cases (M3-M5 and M8-M10) with the most refined grid exhibit an excellent mutual agreement. More specifically, the LES results for model A (cases, M3-M5) show negligible sensitivity to the mesh resolution, thereby indicating that momentum fluxes converge in both the near-wake ($x/D < 5$) and the far-wake ($x/D > 5$) region. A similar trend in the wake predicted by model B suggests that frictional effects of the blades and nacelle can be averaged. However, two-way feedback between the turbine wake and the atmosphere is a primary factor improving the actuator disk model. Interestingly, there is only one grid point across the rotor in case M1 and case M6. Nevertheless, the trend in the velocity profile closely resembles the experimental velocity profile in the near-wake region. Also, it indicates that a dynamic approach of adjusting the thrust coefficient could correct errors at the coarsest resolution profiles. Indeed, Ref [39] had only one grid point across the rotor in which the horizontal grid spacing was 1 km. In cases M2 and M7, there are only three grid points across the rotor in the horizontal direction. The observations suggest that a reinforcement machine learning algorithm maybe developed for adjusting the thrust coefficient dynamically whenever a sufficiently fine grid spacing is not affordable. Thus, our Gaussian ADM coupled with the scale-adaptive turbulence model has the potential to provide relatively more accurate quantitative understanding of the effect of wakes in annual energy production of actual large wind farms. Below, we compare the velocity profiles of the Gaussian ADM (cases M4 and M9), classical ADM (case M11), and wind-tunnel measurement.

3.1.2. Validation of the Gaussian ADM against wind tunnel measurements

In Fig 6, we compare the mean streamwise velocity profiles of present LES, the wind tunnel data [37], and the LES data provided by Ref [9]. When we look at the mean velocity profiles obtained from case M4 and case M9, we see that the result of the Gaussian ADM has a good agreement

Table 1: Numerical setup of all the cases used in the large eddy simulations with different grid resolution for model A, model B and classical ADM. Case M1 to M11 are for single wind turbine while case M12, M13, and M14 are used for wind farm simulation. Here, $\Delta = (\Delta x \Delta y \Delta z)^{1/3}$ and Δ_G is the width of Gaussian kernel. N_{x_2} and N_{x_3} represents the number of grid points in the spanwise and surface-normal direction of the rotor.

Cases	Model	Resolution	N_{x_2}	N_{x_3}	Δ_G/D	Δ/D
case M1	model A	$48 \times 9 \times 16$	1	5	3.23	0.45
case M2	model A	$64 \times 16 \times 24$	3	8	3.23	0.29
case M3	model A	$128 \times 21 \times 36$	3	12	3.23	0.18
case M4	model A	$180 \times 30 \times 48$	5	16	3.00	0.13
case M5	model A	$324 \times 56 \times 72$	9	24	3.00	0.079
case M6	model B	$48 \times 9 \times 16$	1	5	—	0.45
case M7	model B	$64 \times 16 \times 24$	3	8	—	0.29
case M8	model B	$128 \times 21 \times 36$	3	12	—	0.18
case M9	model B	$180 \times 30 \times 48$	5	16	—	0.13
case M10	model B	$324 \times 56 \times 72$	9	24	—	0.079
case M11	classical ADM	$180 \times 30 \times 48$	5	16	1.46	0.13
case M12	classical ADM	$1024 \times 128 \times 144$	10	32	1.45	0.065
case M13	model A	$476 \times 60 \times 72$	5	16	2.40	0.13
case M14	model B	$476 \times 60 \times 72$	5	16	—	0.13

with the experimental data in the *far-wake* ($x/D > 5$) region, which agrees with the outcome of classical ADM that appeared in the literature [40, 30, 10, 31, 41, 42]. However, the Gaussian ADM also accurately captures the velocity distribution in the *near-wake* region ($x/D < 5$). Fig 6 reveals that the actuation of horizontal axis wind turbine acts as a spherical canopy of frictional and pressure drag. Experiments of wind turbines can provide limited measurement results such as velocity and pressure. Our scale-adaptive LES coupled with model A or model B indicates a balance of the efficiency and accuracy in predicting the annual energy production of modern large

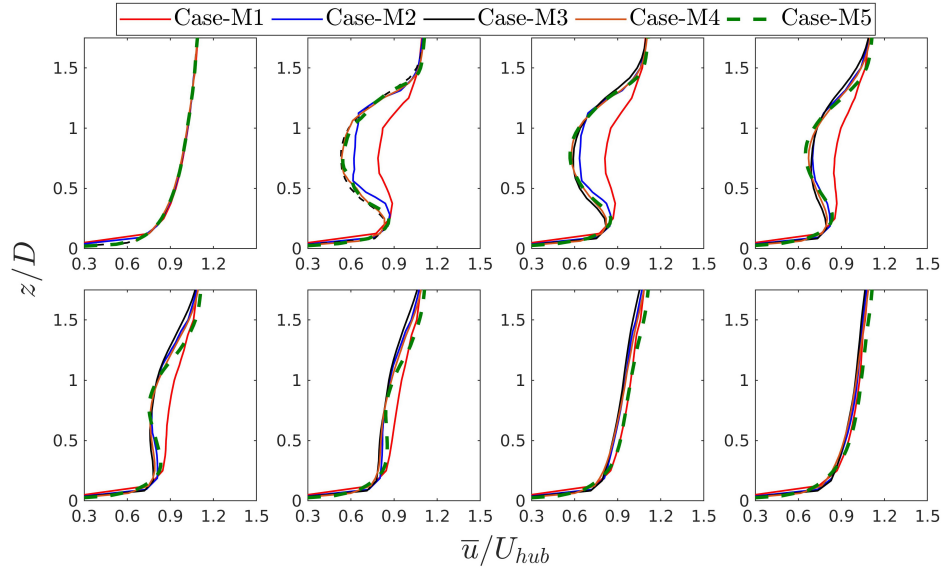


Figure 4: A Comparison of vertical profiles of mean streamwise velocity for five different mesh resolutions in case of model A (see, Table 1).

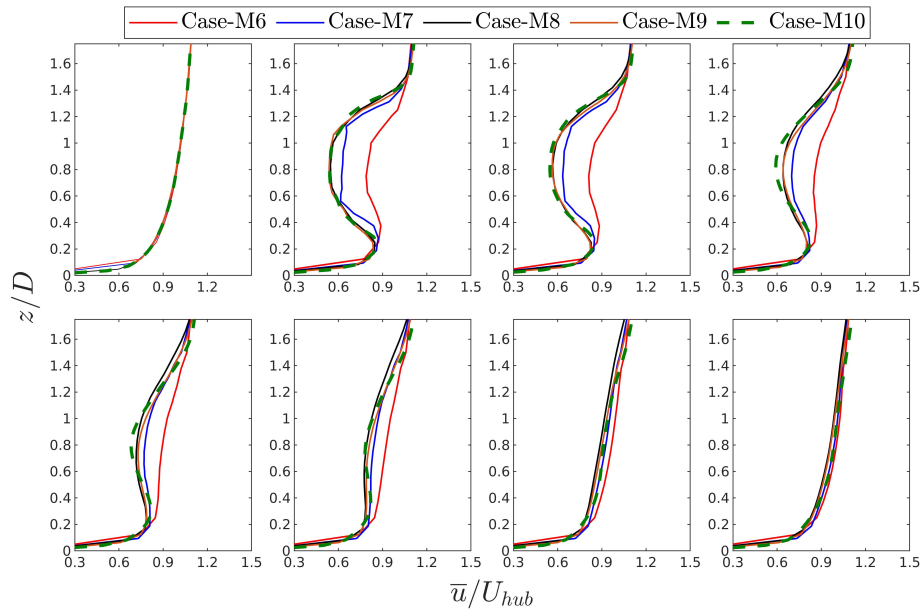


Figure 5: A comparison of vertical profiles of mean streamwise velocity for five different mesh resolution in case of model B (see, Table (1)).

wind farms.

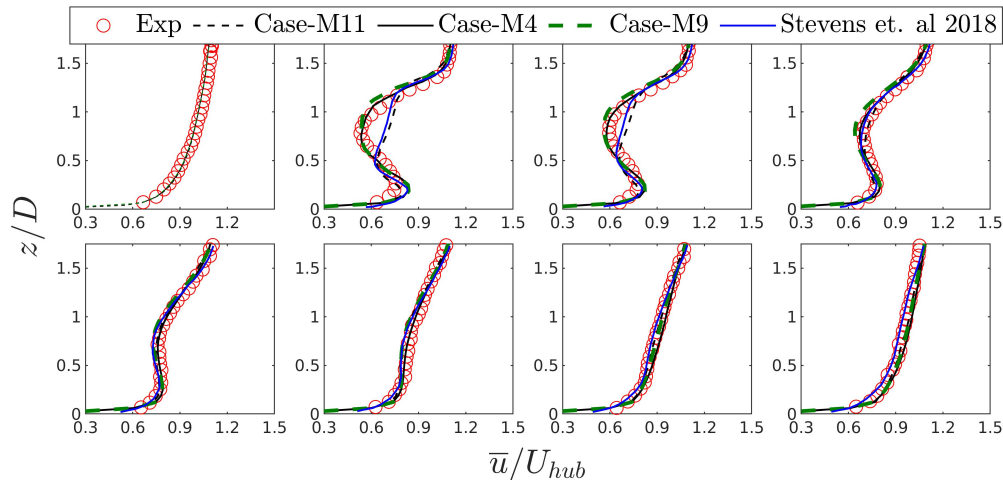


Figure 6: A comparison of vertical profiles of mean streamwise velocity among wind tunnel measurements [37], corresponding LES data [9], and our present LES results for classical ADM, model A and model B.

The interaction of wakes down-wind of a turbine shows a velocity deficit reducing 10%–20% energy production. Here, we discuss the interaction of neutrally stratified atmospheric boundary layer flow over an array of 30 wind turbines by comparing the results of scale-adaptive LES with wind tunnel measurements. It is worth mentioning that wind tunnel measurements are subject to the validity of the Reynolds number similarity theory. However, a wind tunnel validation for physical and dynamical considerations in the scale-adaptive LES of Gaussian ADM helps to understand accurate numerical design of actual wind farms. Figs 7 & 8 show the mean streamwise velocity distribution in the vertical mid-plane of the wind farm at locations, $x/D = 1, 2, 3, 4$, behind the wind turbines. Here, we have compared the velocity profiles of scale-adaptive LES with wind tunnel measurements. We have also employed the classical ADM within our scale-adaptive LES framework and compared the corresponding results with scale-dependent Lagrangian LES coupled with the classical ADM [9]. We find that the velocity profiles obtained with model A and model B have a good agreement with experimental observations [38] in the *near-wake* as well as in the *far-wake* region.

On the other hand, results with classical ADM are as good as previous LES data [9]. We also noticed that the mean profiles obtained with classical ADM significantly improved in the *near-wake* region compared to a standalone wind turbine. This is because assumptions made in ADM closely agree with the wake-layer profile created at the hub height in the large wind farms. This finding is well aligned with the literature [9].

To illustrate the flow adjustment within wind farms, Fig 9 display the vertical profiles of the streamwise velocity and the associated velocity deficit. It is noticeable from the data that flow within the wind farm reached an equilibrium state starting from the fourth row. This result is also in a well agreement with the corresponding wind-tunnel measurements. Fig 9c also indicates that the velocity deficit follows a perfect Gaussian distribution. Again, this indicates a further validation of the assumption made in the Gaussian actuation of the turbine in model A.

To illustrate the gradual decrease of the aerodynamic power available to each turbine, Fig 10 shows the mean streamwise velocity along the top tip, hub height, and bottom tip of wind turbines.

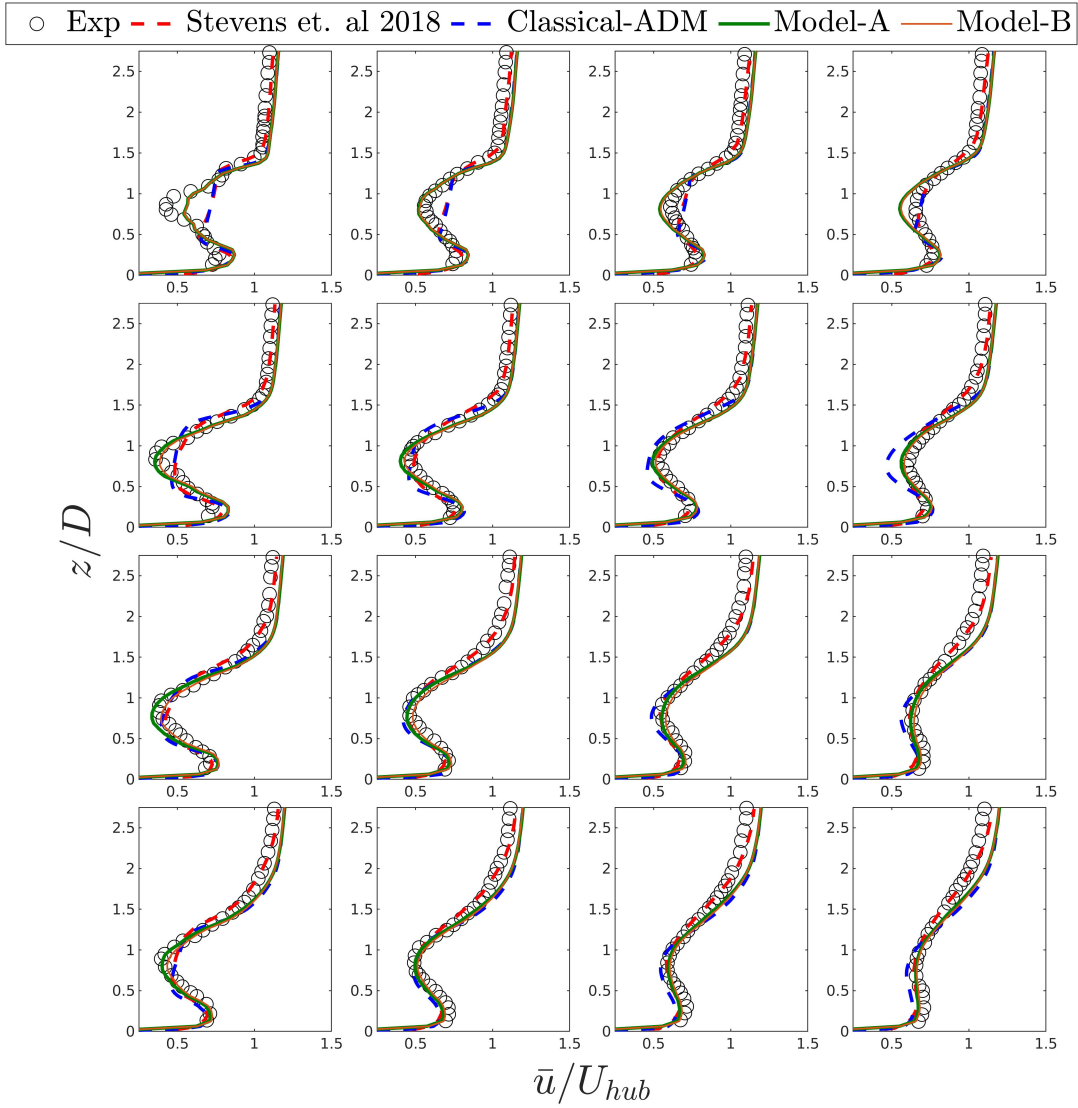


Figure 7: A comparison of vertical profiles of mean streamwise velocity between wind-tunnel measurements [37], corresponding LES data [9] and our present LES for classical ADM, model A, and model B in case of wind farm.

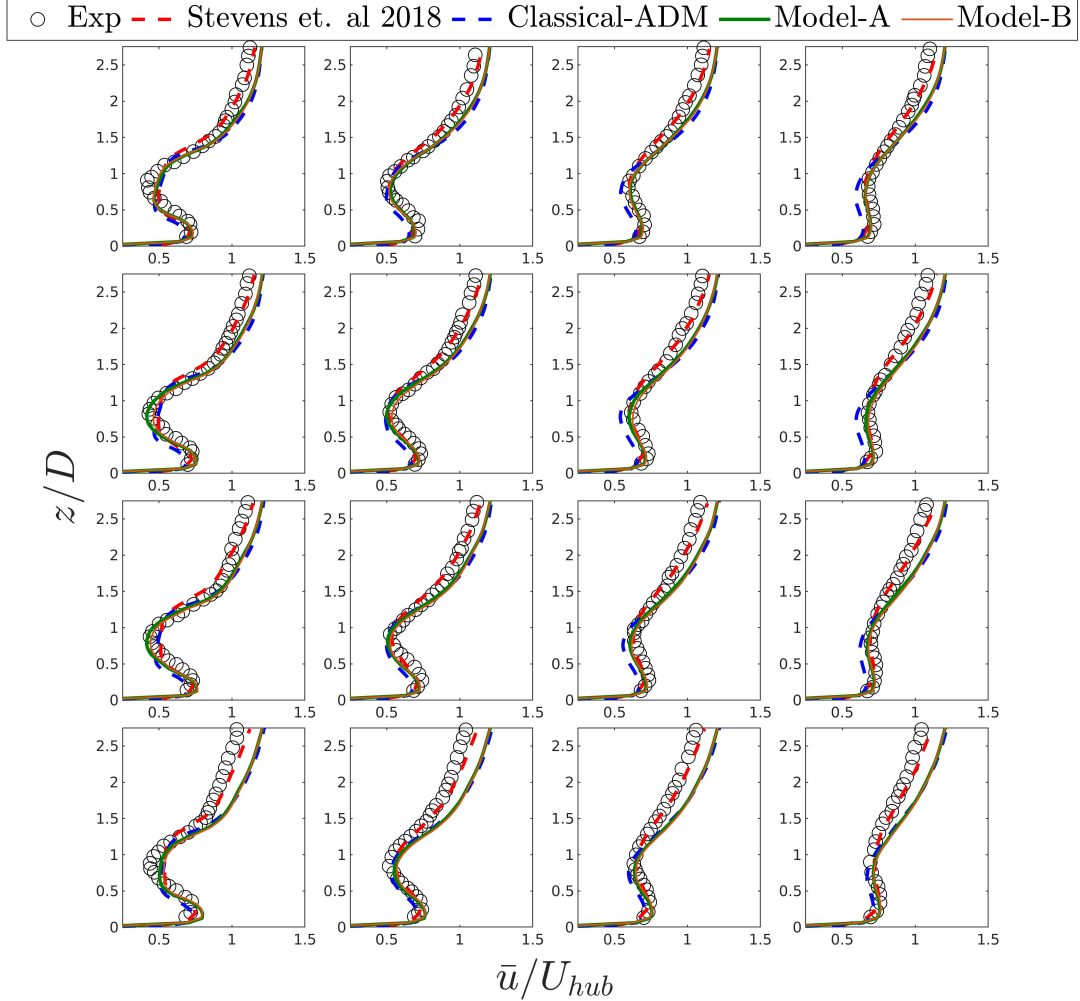


Figure 8: A comparison of vertical profiles of mean streamwise velocity between wind-tunnel measurements [37], corresponding LES data [9] and our present LES for classical ADM, model A, and model B in case of wind farm.

The aerodynamic power of each turbine is proportional to the third power of the velocity. Thus, comparing the wind speeds from LES with wind tunnel measurements is sufficient to validate a trend in the energy production from a numerical wind farm. Furthermore, fig 10 shows that averaged streamwise velocities on the corresponding locations align with the experimental data. It is also worth mentioning that the trend of the decline in aerodynamic power depicted in Fig 10 represents that in the field measurements in the ‘Invenergy Vantage wind farm’ in the state of Washington, USA (see Fig 5 of Ref [41]).

3.2. Turbulence in wind farms

Atmospheric turbulence may increase or decrease the energy production of individual wind turbines. In addition, it impacts loads and fatigue of turbines and may dictate how wind farms would impact their local environment through wake effects and noise propagation [17, 39, 5]. In understanding turbulent flow over surface protuberances, a question often arises: how to characterize turbulent secondary motions quantifying the degree of spatial heterogeneity. Note that the scale-adaptive LES leans on a famous mathematical result. It states that the solution of the

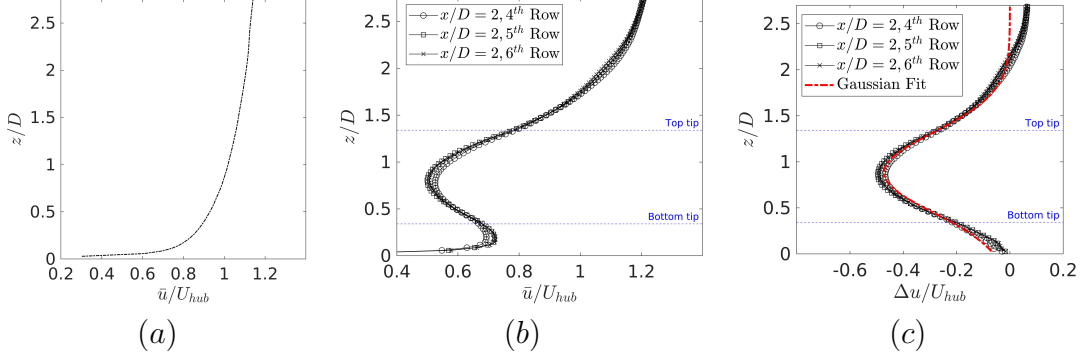


Figure 9: (a) Incoming vertical profile of the stream-wise velocity normalized with its hub-height value; (b) vertical profile of the streamwise velocity in the wake behind turbines on the central column of the 10×3 array at $x/D = 2$ for 4th, 5th, and 6th rows; and (c) vertical profiles of the streamwise velocity deficit, *i.e.* the difference of the data in (a) from that in (b). The corresponding outcome of model B was found similar to that of model A shown here.

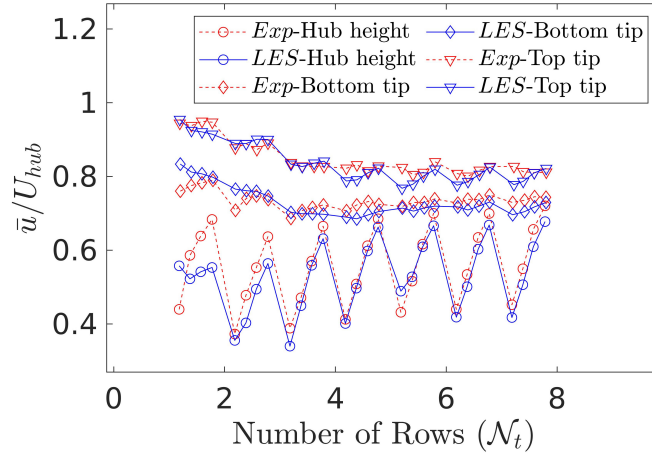


Figure 10: A comparison of the mean stream-wise velocity at top-tip, hub-height, and bottom-tip. The data correspond to velocity at four stream-wise locations: $x/D = 1$, $x/D = 2$, $x/D = 3$, and $x/D = 4$ across the central column and relative to each of the first seven rows of the wind turbine array.

Navier-Stokes equations remains bounded as long as the enstrophy ($0.5|\omega|^2$) of the flow remains bounded [43]. Said another way, the production of vorticity by wind turbines (or other form of surface protuberances) would account for the stresses arising due to correlations among the spatially non-homogeneous mean horizontal and mean vertical velocities. In this section, we consider the wind-tunnel measurements of Reynolds stresses [37] for evaluating the Reynolds stresses, $\tau_{ij}^R = \widetilde{u'_i u'_j}$, resolved with proposed scale-adaptive LES method and analyze the effects of vortex stretching on τ_{ij}^R . Considering turbines as probes of turbulence, we observe that a prolonged flow adjustment above the wind farm correlates with a deepening of atmospheric boundary layer (see Fig 9). Finally, we report relative importance of the dispersive stresses $\tau_{ij}^D = \langle u''_i u''_j \rangle$ over the Reynolds stress τ_{ij}^R , where $\bar{u}_i(\mathbf{x}, t) = \langle \tilde{u}_i \rangle(z) + u''(\mathbf{x}, t) + u'(\mathbf{x}, t)$, $\bar{u}_i(\mathbf{x}) = \langle \tilde{u}_i \rangle(z) + u''(\mathbf{x}, t)$, and $\bar{u}_i(\mathbf{x}, t) = \tilde{u}_i(\mathbf{x}) + u'(\mathbf{x}, t)$.

Fig 11 shows the streamwise turbulence intensity σ/U_{hub} (where $\sigma = \sqrt{\tau_{11}^R}$) for scale-adaptive LES of a standalone wind turbine, using classical ADM, model A, and model B. We have also

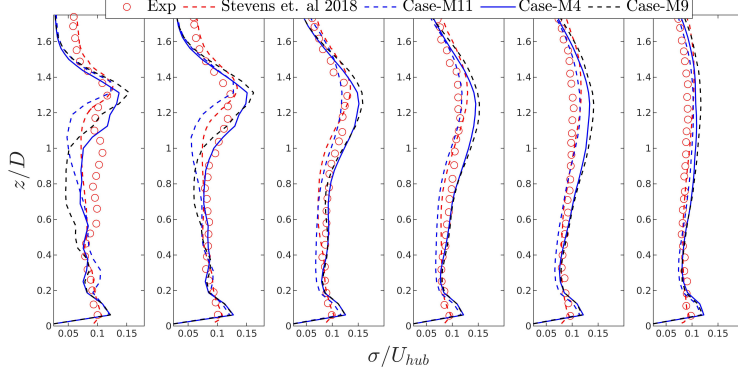


Figure 11: A comparison of turbulence intensity (σ/U_{hub}) among wind-tunnel measurements [37], LES data [9], and our present LES coupled with classical ADM, model A, and model B. The data corresponds to turbulence intensity at various streamwise locations: $x/D = 2$, $x/D = 3$, $x/D = 5$, $x/D = 7$, $x/D = 10$, and $x/D = 14$.

compared the corresponding results with wind-tunnel measurements and the LES data presented by Ref [9]. We chose ($2 < x/D < 7$) for the stresses shown in Fig 11 because it is a critical region for loads on a wind turbine as, in a real wind farm, a downwind turbine may be placed in this region. The maximum enhancement of turbulence intensity seems to be at the top of the wind turbine ($z/D \approx 1.3$) and is consistent with findings that appeared in the experimental investigations in the literature [9, 30]. Numerical results obtained with three models show a similar trend of reaching the maximum value. However, they differ considerably in capturing the vertical distribution of turbulence intensity due to associated assumptions of a model. LES with model A shows a good agreement with the wind tunnel data, while classical ADM and model B slightly underpredicts the turbulence intensity in the *near-wake* region ($x/D < 5$). Nevertheless, all models show a similar profile in the *far-wake* zone, particularly for $x/D > 10$.

Vertical profiles of the shear stress $-\widetilde{u'w'}$ (*i.e.* $-\tau_{13}^R$) appear in Fig 12. For a pedagogical reason, we consider the corresponding result of the actuator disk model with rotation (ADM-R) [30]. One observes that the shear stress has a positive value at the top tip of the wind turbine. Thus, shear production of turbulence in that region entrains high momentum air parcels from aloft and transmits toward the blades (see also [17]). On the other hand, the shear stress is negative below the hub height. Thus, horizontal fluctuations correlate highly with adverse perturbations of vertical velocity near the bottom tip of turbines, $z/D = 0.3$. The outcome of this downward transmission (or ejection) of low momentum air parcels may be a potential source of ground friction velocity u_* . For instance, Ref [44] observed enhanced vertical entrainment of mean energy due to an enhancement of u_* in the presence of surface protrusions.

Here, we briefly evaluate the sensitivity of c_k that appears in Eq (9). Fig 13 shows the diagonal components of the resolved Reynolds stress ($\tau_{11}^R = -\widetilde{u'u'}$, $\tau_{22}^R = -\widetilde{v'v'}$, $\tau_{33}^R = -\widetilde{w'w'}$), and the shear stress ($\tau_{13}^R = -\widetilde{u'w'}$) corresponding to three values of c_k . The vertical profiles of Reynolds stresses depicted in Fig 13 are not drastically sensitive to a choice of c_k . This indicates that a machine learning algorithm can rigorously estimate c_k , if desired. However, the prediction of c_k with isotropic turbulence also seems to be sufficient for the test cases considered in this article.

According to [38], flow in the wind farm can be split into two distinct regions based on the downstream distance needed to reach equilibrium. The region-I ($z/D < 1.34$) – just below the top tip of the wind turbine – directly influences the wind turbines' performance. On the other

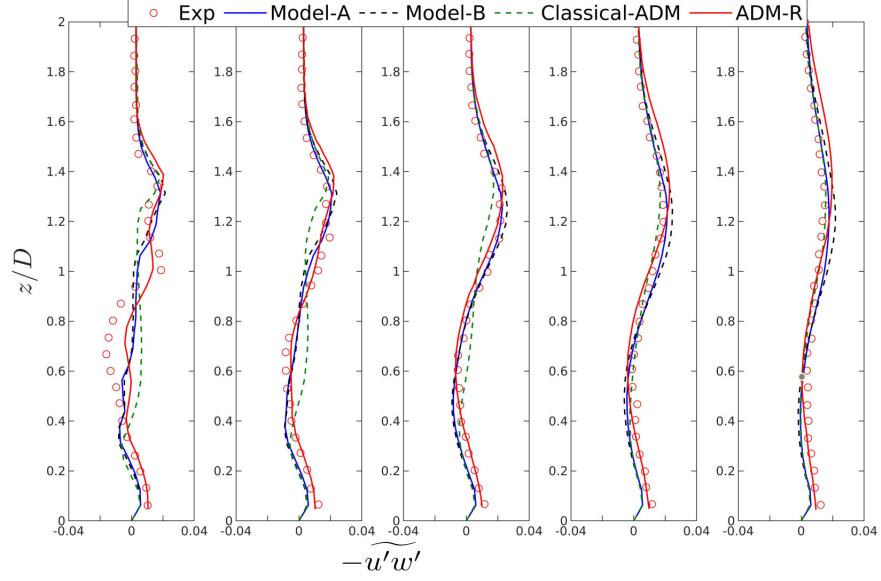


Figure 12: A comparison of kinematic shear stress ($-u'w'$) among wind-tunnel measurements [37], actuator disk with rotation (ADM-R) [30], and our present LES coupled with classical ADM, model A, and model B. The data corresponds to kinematic shear stress at various streamwise locations: $x/D = 2$, $x/D = 3$, $x/D = 5$, $x/D = 7$, and $x/D = 10$.

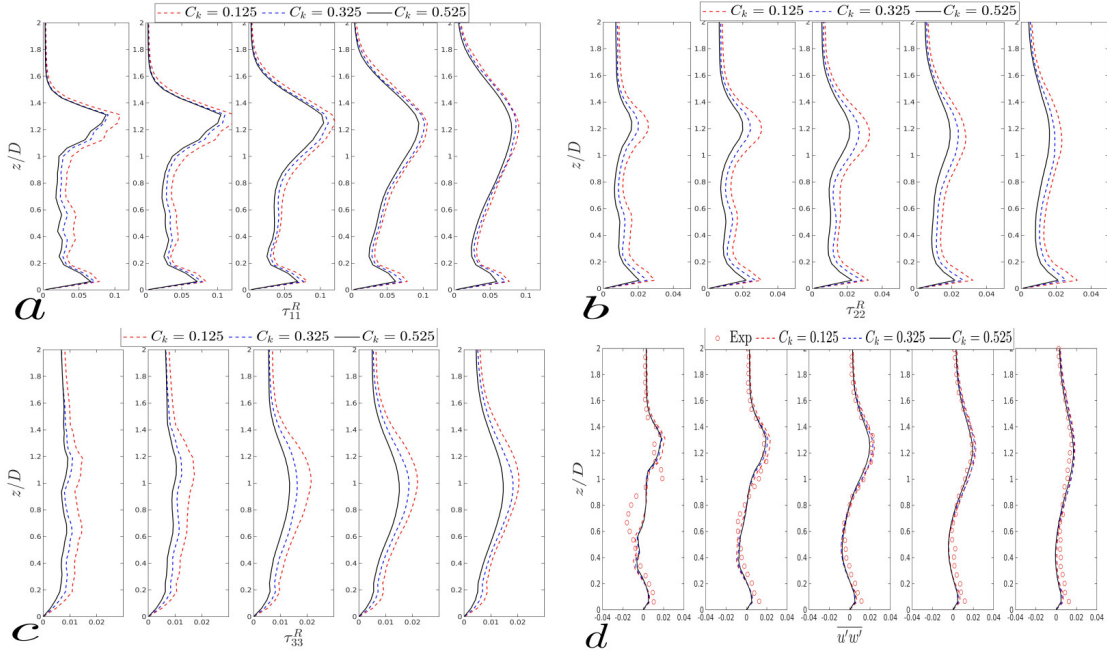


Figure 13: Sensitivity of model constant c_k . Data corresponds to turbulence stresses for three different model coefficient c_k in case of scale-adaptive LES coupled with model-A at various streamwise locations: $x/D = 2$, $x/D = 3$, $x/D = 5$, $x/D = 7$ and $x/D = 10$.

hand, region-II ($z/D > 1.34$) is above the wind turbine's top tip. We collected the instantaneously resolved velocity $\bar{u}_1(\mathbf{x}, t)$ at $x/D = 3$ and near the top tip and the bottom tip, respectively, for each wind turbine. Fig 14 shows the probability density function of normalized $\bar{u}_1(\mathbf{x}, t)$ in region I and region II. The top panel in Fig 14 reveals that flow in region I reaches equilibrium starting from the fourth row, which indicates the quick adjustment of the flow within the wind farm. The bottom panel illustrates the probability density function of streamwise velocity at the top tip (*i.e.* region II) of corresponding wind turbines. Clearly, flow adjustment above the wind farm is prolonged and does not indicate equilibrium in the first four rows and reaches equilibrium far downstream (6th – 7th row) in the wind farm, indicating that different dynamical processes are occurring between two regions, such as mixing and vertical transport. This finding agrees well with relevant experimental outcome [38], thereby suggesting the capability of the scale-adaptive LES using model A. The point at which the flow reaches equilibrium is of significance. For example, a weather prediction model requires the input of a certain parameter treating wind farms as an elevated surface roughness. Such a similarity theory may need to consider the flow adjustments depicted in Fig 14.

Next, we study the effect of dispersive stresses in the wind farm. The dispersive stress mainly originates from roughness elements, and their wakes [45, 46]. Since the presence of a wind turbine array causes significant spatial inhomogeneity, the dispersive stress is predicted to contribute a significant portion to the total shear stress [17]. The study of spatial heterogeneity is of particular relevance because it directly impacts the wind farm's annual energy production. Therefore, it is imperative to consider the dispersive shear stress alongside the Reynolds shear stress to get a complete picture of momentum exchange in a wind farm. Plots of the spatially averaged vertical profiles of the kinetic energy ($k = (1/2)\text{Tr}(\tau_{ij}^R)$), Reynolds shear stress (τ_{13}^R), and dispersive shear stress (τ_{13}^D) for classical ADM, model A, and model B are shown in Fig 15a-b. Model A and model B predicted a maximum of 40% of the dispersive stresses in the wind farm, which is consistent with the findings from other investigator [17, 47]. Dispersive stress is highly influenced by the shape, size, and how the roughness elements are distributed and thus the magnitude of dispersive stress may vary. Hence, analyzing the combined shear stresses with scale-adaptive LES may provide valuable insight into designing an efficient layout of wind farms.

3.3. Flow visualization

Fig 16-18 shows 3D snapshots of iso-vorticity (*i.e.* $(1/2)|\boldsymbol{\omega}|^2$) for Gaussian actuator disk: 'model A' and 'model B'. It is worth mentioning that snapshots of iso-vorticity for the Gaussian ADM (Fig 16) closely resemble the pattern of iso-vorticity predicted with a more sophisticated actuator line model, *e.g.*, Fig 13 of Ref [16]. Considering the overall dynamics of the enstrophy transport equation,

$$\frac{D}{Dt} \left(\frac{1}{2} |\boldsymbol{\omega}|^2 \right) = \boldsymbol{\omega}^T \mathcal{S} \boldsymbol{\omega} + \frac{1}{\mathcal{R}e} \nabla^2 \left(\frac{1}{2} |\boldsymbol{\omega}|^2 \right) - \frac{1}{\mathcal{R}e} \|\nabla \boldsymbol{\omega}\|_1, \quad (15)$$

we understand the overall rate of transfer of energy in wind turbine wakes (see Ch. 5 of Ref [14] for details). It states that the growth rate of enstrophy (*i.e.*, the rotationality of air parcels) is strictly positive if the sum of vortex stretching $\boldsymbol{\omega}^T \mathcal{S} \boldsymbol{\omega}$ and the diffusion of enstrophy $(1/\mathcal{R}e) \nabla^2 (\frac{1}{2} |\boldsymbol{\omega}|^2)$ exceeds the vorticity dissipation $(1/\mathcal{R}e) \|\nabla \boldsymbol{\omega}\|_1$. We know from mathematical analysis (*e.g.*, see [43]) that the regularity and uniqueness of the filtered solution $\bar{\mathbf{u}}(\mathbf{x}, t)$ of the Navier-Stokes equations are guaranteed up to finite time if the enstrophy of the flow is bounded. Splitting the vorticity as $\boldsymbol{\omega} = \bar{\boldsymbol{\omega}} + \boldsymbol{\omega}'$, one would find two transport equations for the filtered and the fluctuating enstrophy $(1/2)|\bar{\boldsymbol{\omega}}|^2$ and $(1/2)|\boldsymbol{\omega}'|^2$, respectively. Thus, a high correlation between $\boldsymbol{\omega}' > 0$ and

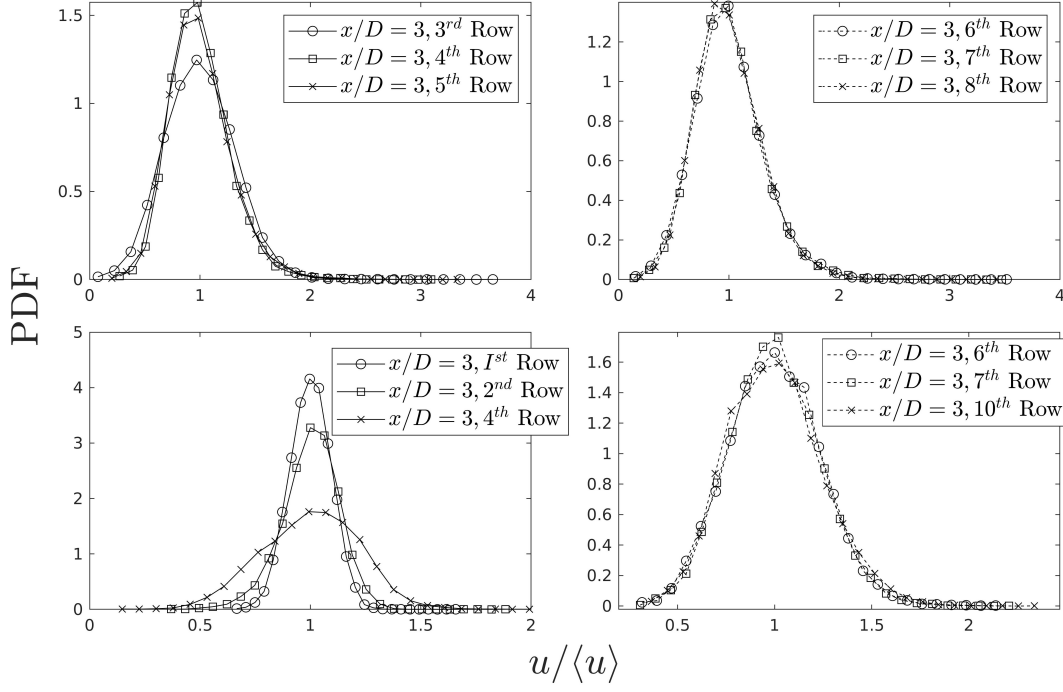


Figure 14: The top panel shows the probability density function (PDF) of instantaneously resolved velocity ($\bar{u}(x, t)$) in region I ($z/D < 1.34$). In contrast, the bottom panel shows PDF of region II ($z/D > 1.34$) in a wind farm.

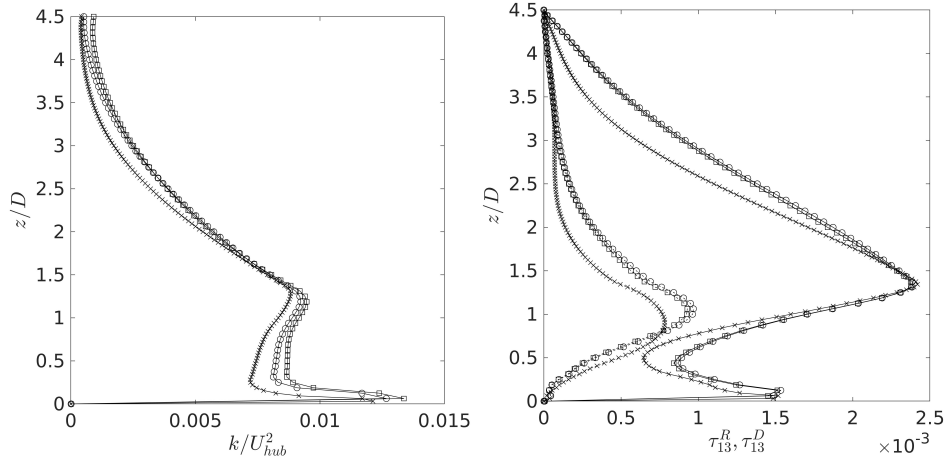


Figure 15: Vertical profiles of horizontally averaged kinetic energy (k), Reynolds (τ_{13}^R), and dispersive (τ_{13}^D) shear stress. Vertical profiles are normalized by streamwise velocity, U_{hub}^2 . Here, solid lines represents Reynolds stress, whereas dashed lines represents corresponding dispersive stress and circle, square, and cross denotes for model A, model B, and classical ADM, respectively.

$D\omega'/Dt > 0$ or between $\omega' < 0$ and $D\omega'/Dt < 0$ corresponds to the growth of disturbances. This brief analysis shows that mathematical knowledge of turbulent flows helps understand the complex nature of wind turbine wakes. In particular, visualization of the enstrophy field illustrates how vortex stretching becomes important to model subgrid-scale turbulence in wind turbine wakes.

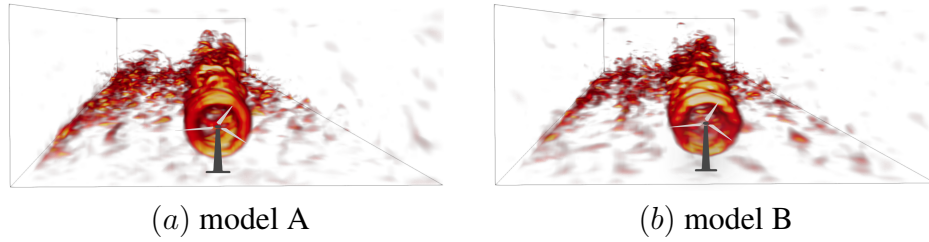


Figure 16: An isosurface plot of the magnitude of vorticity $|\omega|$ computed from the present LES coupled with model A and model B.

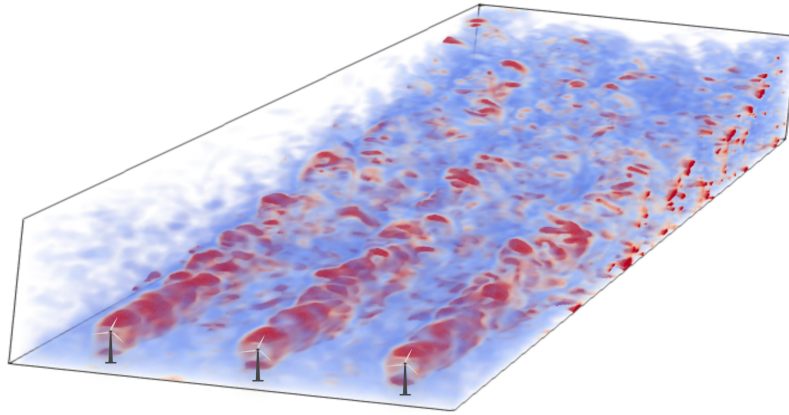


Figure 17: An isosurface plot of the magnitude of vorticity $|\omega|$ computed from the present LES coupled with model A.

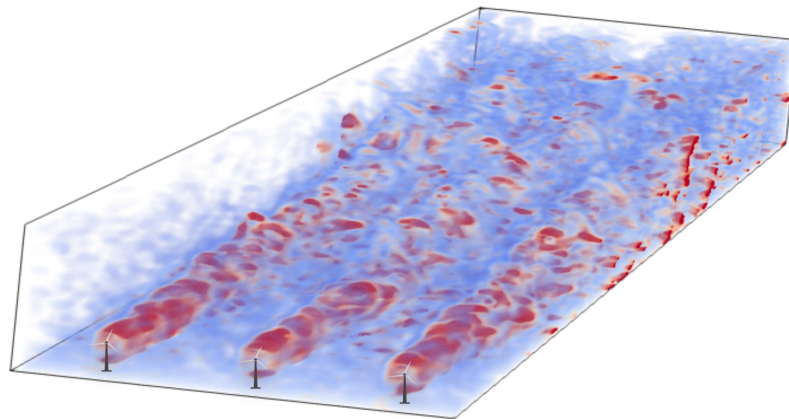


Figure 18: An isosurface plot of the magnitude of vorticity $|\omega|$ computed from the present LES coupled with model B

4. Conclusion and further research directions

This paper presents a detailed analysis of the scale-adaptive large-eddy simulation methodology coupled with the Gaussian actuator disk model for wind farms. To the best of our knowledge, this article contributes significantly, for the first time, toward the development of such a vortex stretching-based subgrid model. A three-dimensional Gaussian kernel is adapted to distribute the thrust force across the rotor. The accuracy and efficiency of the LES framework have been tested

by comparing the model results with wind tunnel measurements and similar LES data. A detailed comparison of average streamwise velocity and Reynolds stresses reveals that the Gaussian actuator disk model performs as accurately as experiments and more sophisticated actuator line models. In addition to comparison with experimental results, we also analyzed those components that directly influence the wind farms' annual energy production (AEP). It is found that model A accurately depicts the streamwise velocity at top tip, hub height, and bottom tip. The corresponding results have an excellent agreement with the wind tunnel data. We employed probability density of instantaneously resolved velocity and observed that model A accurately predicts crucial points in interaction of atmospheric boundary layer with wind farms. Flow visualization reveals that our Gaussian actuator model predicts the wakes qualitatively similar to the actuator line model. Finding suggests that scale-adaptive large-eddy simulation, when coupled with model A, can be a promising solution for accurately assessing the annual energy production.

References

- [1] F. Porté-Agel, M. Bastankhah, S. Shamsoddin, Wind-turbine and wind-farm flows: a review, *Boundary-Layer Meteorology* 174 (1) (2020) 1–59.
- [2] L. M. Miller, D. W. Keith, Climatic impacts of wind power, *Joule* 2 (12) (2018) 2618–2632.
- [3] C. Meneveau, Big wind power: seven questions for turbulence research, *Journal of Turbulence* 20 (1) (2019) 2–20.
- [4] F. Porté-Agel, Y.-T. Wu, C.-H. Chen, A numerical study of the effects of wind direction on turbine wakes and power losses in a large wind farm, *Energies* 6 (10) (2013) 5297–5313.
- [5] M. J. Churchfield, S. Lee, J. Michalakes, P. J. Moriarty, A numerical study of the effects of atmospheric and wake turbulence on wind turbine dynamics, *Journal of turbulence* 13 (2012) N14.
- [6] S. Xie, C. L. Archer, A numerical study of wind-turbine wakes for three atmospheric stability conditions, *Boundary-Layer Meteorology* 165 (1) (2017) 87–112.
- [7] C. L. Archer, A. Vassel-Behagh, C. Yan, S. Wu, Y. Pan, J. F. Brodie, A. E. Maguire, Review and evaluation of wake loss models for wind energy applications, *Applied Energy* 226 (2018) 1187–1207. doi:<https://doi.org/10.1016/j.apenergy.2018.05.085>.
- [8] R. J. Stevens, C. Meneveau, Flow structure and turbulence in wind farms, *Annual review of fluid mechanics* 49 (2017) 311–339.
- [9] R. J. Stevens, L. A. Martínez-Tossas, C. Meneveau, Comparison of wind farm large eddy simulations using actuator disk and actuator line models with wind tunnel experiments, *Renewable energy* 116 (2018) 470–478.
- [10] F. Porté-Agel, Y.-T. Wu, H. Lu, R. J. Conzemius, Large-eddy simulation of atmospheric boundary layer flow through wind turbines and wind farms, *Journal of Wind Engineering and Industrial Aerodynamics* 99 (4) (2011) 154–168.
- [11] J. M. Alam, A. Afanassiev, J. Singh, Characterizing impacts of atmospheric turbulence on wind farms through large eddy simulation (les), in: *International Conference on Offshore Mechanics and Arctic Engineering*, Vol. 58899, American Society of Mechanical Engineers, 2019, p. V010T09A052.
- [12] J. Garratt, *The Atmospheric Boundary Layer*, Cambridge University Press, 1994.
- [13] R. Stoll, J. A. Gibbs, S. T. Salesky, W. Anderson, M. Calaf, Large-eddy simulation of the atmospheric boundary layer, *Boundary-Layer Meteorology* 177 (2) (2020) 541–581.
- [14] P. A. Davidson, *Turbulence: an introduction for scientists and engineers*, Oxford university press, 2015.
- [15] M. Bhuiyan, A. Samad, J. M. Alam, Scale-adaptive turbulence modeling for les over complex terrain, *Engineering with Computers* (2020) 1–13.

- [16] H. Sarlak, C. Meneveau, J. N. Sørensen, Role of subgrid-scale modeling in large eddy simulation of wind turbine wake interactions, *Renewable Energy* 77 (2015) 386–399.
- [17] M. Calaf, C. Meneveau, J. Meyers, Large eddy simulation study of fully developed wind-turbine array boundary layers, *Physics of fluids* 22 (1) (2010) 015110.
- [18] J. Smagorinsky, General circulation experiments with the primitive equations: I. the basic experiment, *Monthly weather review* 91 (3) (1963) 99–164.
- [19] J. W. Deardorff, Stratocumulus-capped mixed layers derived from a three-dimensional model, *Boundary-layer meteorology* 18 (4) (1980) 495–527.
- [20] J. Hunt, Length scales in stably stratified turbulent flows and their use in turbulence models, *Stably stratified flow and dense gas dispersion*.
- [21] K. Horiuti, A proper velocity scale for modeling subgrid-scale eddy viscosities in large eddy simulation, *Physics of Fluids A: Fluid Dynamics* 5 (1) (1993) 146–157.
- [22] V. Canuto, Y. Cheng, Determination of the smagorinsky–lilly constant c_s , *Physics of Fluids* 9 (5) (1997) 1368–1378.
- [23] F. Porté-Agel, A scale-dependent dynamic model for scalar transport in large-eddy simulations of the atmospheric boundary layer, *Boundary-Layer Meteorology* 112 (1) (2004) 81–105.
- [24] M. Germano, U. Piomelli, P. Moin, W. H. Cabot, A dynamic subgrid scale eddy viscosity model, *Physics of Fluids A* 3 (7) (1991) 1760–1775.
- [25] C. Meneveau, T. S. Lund, W. H. Cabot, A lagrangian dynamic subgrid-scale model of turbulence, *Journal of fluid mechanics* 319 (1996) 353–385.
- [26] F. Porté-Agel, C. Meneveau, M. B. Parlange, A scale-dependent dynamic model for large-eddy simulation: application to a neutral atmospheric boundary layer, *Journal of Fluid Mechanics* 415 (2000) 261–284.
- [27] E. Bou-Zeid, C. Meneveau, M. Parlange, A scale-dependent lagrangian dynamic model for large eddy simulation of complex turbulent flows, *Physics of fluids* 17 (2) (2005) 025105.
- [28] R. Stoll, F. Porté-Agel, Dynamic subgrid-scale models for momentum and scalar fluxes in large-eddy simulations of neutrally stratified atmospheric boundary layers over heterogeneous terrain, *Water Resources Research* 42 (1).
- [29] F. Wan, F. Porté-Agel, R. Stoll, Evaluation of dynamic subgrid-scale models in large-eddy simulations of neutral turbulent flow over a two-dimensional sinusoidal hill, *Atmospheric Environment* 41 (13) (2007) 2719–2728.
- [30] Y.-T. Wu, F. Porté-Agel, Large-eddy simulation of wind-turbine wakes: evaluation of turbine parametrisations, *Boundary-layer meteorology* 138 (3) (2011) 345–366.

- [31] Y.-T. Wu, F. Porté-Agel, Simulation of turbulent flow inside and above wind farms: model validation and layout effects, *Boundary-layer meteorology* 146 (2) (2013) 181–205.
- [32] C. R. Shapiro, D. F. Gayme, C. Meneveau, Filtered actuator disks: Theory and application to wind turbine models in large eddy simulation, *Wind Energy* 22 (10) (2019) 1414–1420.
- [33] A. Crespo, J. Hernandez, S. Frandsen, Survey of modelling methods for wind turbine wakes and wind farms, *Wind Energy: An International Journal for Progress and Applications in Wind Power Conversion Technology* 2 (1) (1999) 1–24.
- [34] M. K. Hossen, A. Mulayath-Variyath, J. Alam, Statistical analysis of dynamic subgrid modeling approaches in large eddy simulation (2021). doi:10.20944/preprints202109.0438.v1.
URL <https://doi.org/10.20944/preprints202109.0438.v1>
- [35] J. M. Alam, L. P. Fitzpatrick, Large eddy simulation of flow through a periodic array of urban-like obstacles using a canopy stress method, *Computers & Fluids* 171 (2018) 65–78.
- [36] L. P. Chamorro, F. Porté-Agel, A wind-tunnel investigation of wind-turbine wakes: boundary-layer turbulence effects, *Boundary-layer meteorology* 132 (1) (2009) 129–149.
- [37] L. P. Chamorro, F. Porté-Agel, Effects of thermal stability and incoming boundary-layer flow characteristics on wind-turbine wakes: a wind-tunnel study, *Boundary-layer meteorology* 136 (3) (2010) 515–533.
- [38] L. P. Chamorro, F. Porté-Agel, Turbulent flow inside and above a wind farm: a wind-tunnel study, *Energies* 4 (11) (2011) 1916–1936.
- [39] S. B. Roy, Simulating impacts of wind farms on local hydrometeorology, *Journal of Wind Engineering and Industrial Aerodynamics* 99 (4) (2011) 491–498.
- [40] A. Jimenez, A. Crespo, E. Migoya, J. García, Advances in large-eddy simulation of a wind turbine wake, in: *Journal of Physics: Conference Series*, Vol. 75, IOP Publishing, 2007, p. 012041.
- [41] X. Yang, F. Sotiropoulos, On the predictive capabilities of les-actuator disk model in simulating turbulence past wind turbines and farms, in: *2013 American Control Conference*, IEEE, 2013, pp. 2878–2883.
- [42] D. Yang, C. Meneveau, L. Shen, Large-eddy simulation of offshore wind farm, *Physics of Fluids* 26 (2) (2014) 025101.
- [43] C. Foias, R. Temam, Gevrey class regularity for the solutions of the navier-stokes equations, *Journal of Functional Analysis* 87 (2) (1989) 359–369.
- [44] L. Liu, R. J. A. M. Stevens, Enhanced wind-farm performance using windbreaks, *Phys. Rev. Fluids* 6 (2021) 074611.

- [45] T. O. Jelly, A. Busse, Reynolds number dependence of reynolds and dispersive stresses in turbulent channel flow past irregular near-gaussian roughness, *International Journal of Heat and Fluid Flow* 80 (2019) 108485.
- [46] D. Toussaint, F. Chedevergne, O. Léon, Analysis of the different sources of stress acting in fully rough turbulent flows over geometrical roughness elements, *Physics of Fluids* 32 (7) (2020) 075107.
- [47] D. Poggi, G. Katul, J. Albertson, A note on the contribution of dispersive fluxes to momentum transfer within canopies, *Boundary-layer meteorology* 111 (3) (2004) 615–621.